GFZ

Helmholtz-Zentrum
POTSDAM

Originally published as:

Effects of temperature and pressure on the optical and vibrational properties of thermoelectric SnSe

Ilias Efthimiopoulos,[1, *] Matthias Berg,[2] Annika Bande,[2] Ljiljana Puskar,[2] Eglof Ritter,[3] Wei Xu,[4] Augusto Marcelli,[5, 6] Michele Ortolani,[7] Martin Harms,[1] Jan Müller,[1] Sergio Speziale,[1] Monika Koch-Müller,[1] Yong Liu,[8] Li-Dong Zhao,[9] and Ulrich Schade[2]

[1] *GFZ German Research Centre for Geosciences, Telegrafenberg, 14473 Potsdam, Germany*
[2] *Institute of Methods for Material Development, Helmholtz-Zentrum Berlin für Materialien und Energie, Albert-Einstein-Strasse 15, 12489 Berlin, Germany*
[3] *Institute of Biology, Humboldt-Universität zu Berlin, Invalidenstrasse 42, 10115 Berlin, Germany*
[4] *Beijing Synchrotron Radiation Facility, Institute of High Energy Physics, Chinese Academy of Sciences, 100049 Beijing, PR China*
[5] *INFN-Laboratori Nazionali di Frascati, Via E. Fermi 40, Frascati, 00044, Italy*
[6] *RICMASS, Rome International Center for Materials Science Superstripes, Via dei Sabelli 119A, 00185 Rome, Italy*
[7] *Department of Physics, University of Rome La Sapienza, P.le A. Moro 2, 00185 Rome, Italy*
[8] *AECC-Beijing Institute of Aeronautical Materials, No. 8 Hangcai Avenue, Huanshancun, Haidian District, 100095 Beijing, PR China*
[9] *School of Materials Science and Engineering, No. 37 Xueyuan Road, Haidian District, Beihang University, 100191 Beijing, PR China*
(Dated: February 4, 2019)

We have conducted a comprehensive investigation of the optical and vibrational properties of the binary semiconductor SnSe as a function of temperature and pressure by means of experimental and *ab initio* probes. Our high-temperature investigations at ambient pressure have successfully reproduced the progressive enhancement of free carrier concentration upon approaching the h$Pnma \rightarrow Bbmm$ transition, whereas the pressure-induced $Pnma \rightarrow Bbmm$ transformation at ambient temperature, accompanied by an electronic semiconductor$\rightarrow$semi-metal transition, has been identified for bulk SnSe close to 10 GPa. Modelling of the Raman-active vibrations revealed that three-phonon anharmonic processes dominate the temperature-induced mode frequency evolution. In addition, SnSe was found to exhibit a pressure-induced enhancement of the Born effective charge. Such behavior is quite unique and cannot be rationalized within the proposed effective charge trends of binary materials under pressure.

---

* iliefthi@gfz-potsdam.de

I. INTRODUCTION

Identifying materials for the renewable energy sector constitutes one of the major materials-oriented research goals worldwide. Among the various alternatives being investigated, thermoelectric materials, i.e. compounds which can convert heat to electricity and vice versa, hold a prominent position [1–5]. The thermoelectric efficiency of a given material can be quantified by the dimensionless thermoelectric figure of merit ZT calculated from the following formula:

$$ZT = \frac{S^2 \sigma T}{\kappa} \tag{1}$$

where S is the Seebeck coefficient, σ the electrical conductivity, κ the thermal conductivity, and T the temperature. The thermal conductivity κ can in turn split into two components: the electronic thermal conductivity part κ_{el}, which indicates the heat carried by electrons, and the lattice thermal conductivity constituent κ_{lat}, which denotes the heat carried by the crystal phonons, i.e. $\kappa = \kappa_{el} + \kappa_{lat}$. The former part κ_{el} is dominant in metals, whereas κ_{lat} generally prevails in semiconductors.
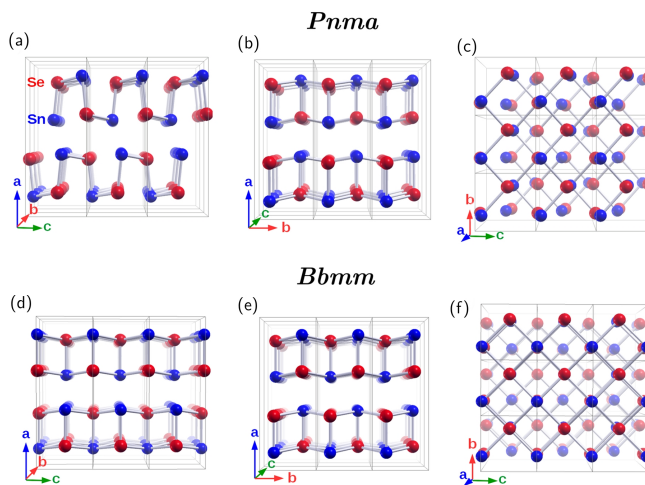
FIG. 1: The structure of SnSe at ambient conditions [SG *Pnma*, $Z = 4$, (a)-(c)] and its high-temperature/ high-pressure phase [SG *Bbmm*, $Z = 4$, (d)-(f)] projected in different crystallographic directions. The Sn and Se atoms are drawn as blue and red spheres, respectively. The black solid parallelepipeds depict unit cells. The crystal structures have been visualized with the program XCrySDen [6].

Recently, a record-high thermoelectric figure of merit ($ZT = 2.6\pm3$) was demonstrated for the binary semiconductor SnSe at temperatures of 923 K [7], possibly paving the way to develop thermoelectric devices for energy harvesting which consist of simple and stable compounds built up by cheap earth-abundant elements, since present thermoelectric stages are often based on rare elements such as Bi and Te [8]. The intriguing thermoeletric properties of SnSe arise mainly from the (ultra)low thermal conductivity inherent to its anisotropic structure [7, 9–11]. At ambient conditions, SnSe crystallizes in a layered orthorhombic phase [space group (SG) *Pnma*, $Z = 4$, Fig. 1] [12, 13]. The structure can be regarded as a distorted variant of the NaCl-type structure, and it comprises of Sn-Se 'corrugated' layers stacked along the a-axis. Upon heating above $\sim$800 K, SnSe is known to adopt another, more symmetric orthorhombic phase above 800 K (SG *Bbmm*, $Z = 4$, Fig. 1) [12–14]; we note that SG *Bbmm* is a different setting of the more commonly used SG *Cmcm* (No. 63), with the *Bbmm* crystal axes ordered in the same way as the starting *Pnma* phase. This high-temperature *Bbmm* modification of SnSe displays the aforementioned excellent thermoelectric properties [7]. Several investigations have revealed that the extremely high thermoelectric efficiency of SnSe is primarily derived from its low κ_{lat} at high temperatures, stemming in turn from the large phonon anharmonicity present in the *Pnma*-SnSe and the high-T *Bbmm*-SnSe modifications [7, 9–11, 15–19]. A hindering factor for exploiting this material for device applications, however, is that SnSe appears to be thermally unstable [20].

Except from the effect of temperature, the layered *Pnma* structure implies that SnSe is susceptible to strain. Indeed, it was shown that SnSe undergoes a second-order phase transition from the starting *Pnma* phase towards a *Bbmm* modification close to 10.5 GPa at ambient temperature [21]. This structural transition is also accompanied by a concurrent electronic transition, from the starting semiconducting towards a semi-metallic behavior [19, 22],

which in turn affects directly the thermoelectric properties of SnSe (eq. 1) [19, 23–25]. For the sake of completeness, we mention that further compression leads SnSe towards a metallic CsCl-type structure between 30-40 GPa [26, 27]. Given that the high-temperature and (first) high-pressure modification of SnSe have the same space group, it was proposed that pressure can effectively lower the $Pnma \rightarrow Bbmm$ transition temperature [10, 11, 15–19, 25, 28].

Since phonons are expected to constitute the dominant mechanism for the (lattice) thermal conductivity in SnSe, and given their sensitivity to changes in interatomic bonding due to the reported structural transitions, it becomes imperative to explore their temperature- and pressure-dependent behavior in detail, as a means of linking the relevant anharmonic processes to the thermoelectric properties of SnSe. With the exception of a recent high-temperature Raman study [29], there are no experimental far-infrared (FIR) or Raman investigations focussing on the temperature- and pressure-induced phase transitions in bulk SnSe. This lack of data prompted us to conduct a comprehensive high-temperature and high-pressure study on a bulk SnSe single-crystalline sample by a combination of experimental FIR reflectance, FIR absorbance, and Raman spectroscopic probes, complemented by first-principles calculations within the framework of hybrid density functional theory (DFT). Out of these investigations we manage to unravel the effect of pressure and temperature on the optical, vibrational, and electronic properties of SnSe across the $Pnma \rightarrow Bbmm$ transition, as well as an estimate of the mode-specific phonon anharmonicity contributions to the detected Raman-active vibrations of SnSe.

The paper is organized as follows: after the detailing of the experimental (Sec.II A) and computational methods (Sec.II B), we present our high-temperature experimental FIR reflectance and Raman results at ambient pressure on pristine SnSe (Sec.III A). Furthermore, our high-pressure structural, spectroscopic, and computational investigations at ambient temperature are discussed and compared (Sec.III B). The phonon anharmonicity of the $Pnma$-SnSe Raman-active modes is then evaluated (Sec.III C), with the calculated optical properties as a function of pressure (Sec.III D) being presented before summarizing our conclusions (Sec.IV). Finally, the effect of n- and p-type doping on the vibrational and optical properties of SnSe is examined in the *Appendix*.

II. METHODS

A. Experimental details

The SnSe samples examined here were available as impurity-free single crystals. Details of the synthesis and characterization can be found elsewhere [7, 30, 31].

The high-temperature quasi normal-incidence FIR reflectance spectra were acquired from the polished bc-cleavage plane of SnSe single crystals with polarized infrared synchrotron radiation from the BESSY II storage ring within the 295-845 K temperature range. The samples were placed inside a custom-built optical setup, coupled to a Vertex 80v Bruker FTIR spectrometer, allowing for the precise measurement of the specular reflectance at variable temperatures with a 6.5° angle of incidence and a 12° opening angle for the incident IR beam. The sample environment was purged continuously with nitrogen, in order to prevent decomposition and/or oxidation of SnSe during the high-T experiments [20].

The high-temperature Raman measurements on unoriented SnSe single crystals were conducted with a Horiba Jobin Yvon LabRam HR800 VIS spectrometer and a diode-pumped solid-state laser with excitation wavelength $\lambda = 473$ nm, and within the 100-700 cm^{-1} frequency range. The samples were placed inside a Linkam THMS600 stage purged continuously with nitrogen and/or argon gas for reasons explained above. The thermocouple readout temperature has been corrected with an empirical formula, derived from the melting points of different salts and the freezing point of water [32, 33].

The high-pressure measurements at ambient temperature were conducted with gasketed diamond anvil cells (DACs) equipped with low-fluorescence type II diamonds of 400 μm culet diameters. Rhenium gaskets were preindented to a 35-40 μm thickness, with holes of 150-200 μm diameters acting as sample chambers in separate experimental runs. Argon served as a pressure transmitting medium (PTM), whereas the ruby fluorescence method was employed for pressure calibration [34] in all experiments.

The high-pressure Raman spectra on unoriented SnSe single crystals with typical dimensions of 50 x 50 μm^2 were collected in the 100-700 cm^{-1} frequency range ($\lambda = 473$ nm and $\lambda = 633$ nm). Angle-resolved high-pressure X-ray diffraction (XRD) measurements were performed on polycrystalline SnSe powder (ground from single crystals) at the Extreme Conditions Beamline P02.2 of PETRA III (Hamburg, Germany) [35] with an incident X-ray wavelength $\lambda = 0.29$ Å and a beam size of 2 μm $\times$ 2 μm. Two-dimensional XRD patterns were collected with a fast flat panel detector XRD1621 from PerkinElmer (2048 pixels $\times$ 2048 pixels with 200 μm pixel size) and processed with the FIT2D software [36]. Refinements were performed using the GSAS+EXPGUI software packages [37]. Pressure in the XRD run was additionally calibrated using equation of state (EoS) of the argon PTM [38, 39].

B. Computational details

All DFT calculations were performed with the CRYSTAL14 package of programs [40, 41]. PBEsol0 [42–44], the hybrid version (25% Hartree-Fock exchange) of the solid-state revision of the Perdew-Burke-Ernzerhof generalized gradient approximation exchange-correlation functional, is used in conjunction with an all-electron 9-7631-511d Gaussian basis set for Se [45] and a fully-relativistic effective core potential (ECP) plus valence Gaussian basis set ECP28MDF-411-51d for Sn [46, 47]. The basis set for Se adapts the atomic version by Towler [45], from which the most diffuse sp-function was deleted and an additional d-function was added. The ECP and basis set for Sn originate from a version by Baranek [46]. For the present work, the exponents of the outermost sp and d functions within the valence contraction shells of both sets were optimized at the PBEsol level of theory using the experimental ($T = 100$ K) crystal structure of SnSe [13]. The full basis set parameters are reported within the Supplement [48].

The accuracy of the Coulomb and exchange integral series is controlled by the five TOLINTEG parameters 10, 10, 10, 10 and 20. The default integration grid was used (XLGRID). The **k**-space was sampled on a 12×12×12 Monkhorst-Pack mesh. Total energies were converged to 10^{-8} a.u. in structure optimization and to 10^{-10} a.u. in phonon calculations [49, 50].

Full structure optimizations under external hydrostatic pressures [51] were performed successively for pressures spanning from 0 to 20 GPa with an increment of 1 GPa, with tight convergence (TOLDEG = 0.00003, TOLDEX = 0.00004) and trust-radius parameters (MAXTRADIUS = 0.1, TRUSTRADIUS = 0.01). We should note that while the primitive and crystallographic unit cells are equivalent for the ambient-pressure $Pnma$-SnSe phase, this is not the case for the high-T/P $Bbmm$-SnSe modification. In order to keep the numerical errors for the calculation of both SnSe phases comparable, the $Bbmm$ structures were calculated within the primitive unit cell of their $Pnma$ subgroup, by constraining the $z_{Sn} = 0$ and $z_{Se} = 0.5$ atomic coordinates.

Dielectric constants, Born effective charges, IR and Raman phonon intensities were calculated via the coupled perturbed Kohn-Sham (CPKS) method [52–55]. Spectral functions employ Lorentzian broadening for each oscillator, where phenomenological broadening parameters of 5 cm^{-1} were used for all modes of the $Bbmm$-SnSe polymorph, and for the b- and c-axis vibrations of the $Pnma$-SnSe phase. The broadening parameters for the a-axis modes of $Pnma$-SnSe were set to 2.0 cm^{-1}, 7.0 cm^{-1}, and 2.5 cm^{-1} in order of increasing frequency, as guided by the Lorentz fit to the experimental room temperature IR reflectance data [48]. The program XCrySDen [6] has been used for the visualization of the crystal structures and the phonon eigenvectors presented in this work.

III. RESULTS AND DISCUSSION

A. Optical and vibrational properties of SnSe as a function of temperature

In Fig. 2 we plot the measured FIR reflectance spectra of SnSe at various temperatures along the two different $Pnma$ b- and c-crystal axes (Fig. 1). The ambient temperature (295 K) reflectance spectra of SnSe (Fig. 2), as well as the respective fits with the Drude-Lorentz model, are in very good agreement with earlier results [48, 56, 57] (Table S1 in SI [48]). Upon increasing temperature above ∼500 K, we observe that the maximum of the SnSe FIR reflectance for both axial orientations is gradually increasing towards lower frequencies, indicative of a progressive increase in the (thermally activated) free carrier concentration in the b- and c-directions (i.e. within the Sn-Se layers, Fig. 1). Such observation is in excellent agreement with the reported temperature-induced evolution of electrical conductivity in this material along these crystallographic axes [7, 58, 59]. Furthermore, such FIR reflectance increase for frequencies below 100 cm^{-1} indicates that a 'true' Drude term is not present in the SnSe optical conductivity, therefore the free electron scattering rate in SnSe should be fairly high. This fact confirms that the free electron contribution to the thermal conductivity should not impact the thermoelectric properties of SnSe, as already discussed in Ref. 7.

Interestingly, the reported T-induced $Pnma \rightarrow Bbmm$ transition close to 800 K [12–14, 59] does not appear to have any noticeable effect on the FIR reflectance of SnSe (Fig. 2). Attempts to fit the 845 K FIR reflectance spectrum with the Drude-Lorentz model revealed the presence of an additional TO phonon at ∼140 cm^{-1} along the b-axis [48]; a more detailed quantitative description of the T-induced FIR reflectance behavior is hindered, however, due to (a) the inherent T-induced broadening and (b) the screening of the detected FIR phonons from the increasing free carrier concentration.

We turn next to our high-temperature Raman investigations on SnSe. For the $Pnma$-SnSe structure, group theory predicts a total sum of 7 IR- and 12 Raman (R)-active modes at the center of the Brillouin zone Γ [56, 60]:

$$\begin{aligned} \Gamma = 3B_{1u}(IR) + B_{2u}(IR) + 3B_{3u}(IR) \\ + 4A_g(R) + 2B_{1g}(R) + 4B_{2g}(R) + 2B_{3g}(R) \end{aligned} \tag{2}$$
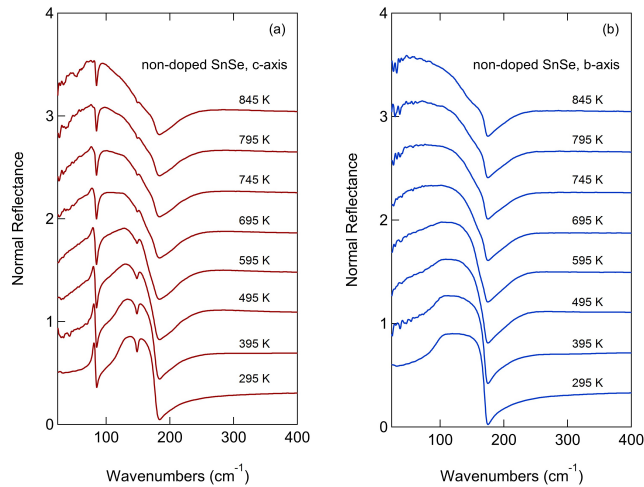
FIG. 2: Experimental FIR reflectance spectra measured with the incident radiation along the (a) c- and (b) b-axes of pristine/non-doped SnSe at various temperatures. The spectra have been shifted vertically by 0.4 for clarity.

whereas for the high-temperature/high-pressure $Bbmm$-SnSe modification, one expects a total sum of 3 IR- and 6 Raman-active modes [56, 60]:

$$\Gamma = B_{1u}(IR) + B_{2u}(IR) + B_{3u}(IR) \\ + 2A_g(R) + 2B_{1g}(R) + 2B_{2g}(R) \tag{3}$$

In Fig. 3 we plot the measured Raman spectra of SnSe at various temperatures. Since the uppermost $Pnma$-SnSe Raman-active mode frequencies are expected close to 200 cm^{-1} [56, 61, 62], the presented Raman spectra are displayed within the 80-250 cm^{-1} frequency range for convenience. The Raman spectrum of $Pnma$-SnSe measured at ambient conditions exhibits three Raman-active vibrations at $\sim$105 cm^{-1} (B$_{3g}^2$) ,$\sim$129 cm^{-1} (A$_g^3$), and at $\sim$149 cm^{-1} (A$_g^4$), consistent with earlier reports [56, 61, 62]. We use the same notation for the observed Raman-active vibration as for our DFT-calculated phonon eigenvectors [48]. Upon increasing temperature, both of the A$_g$ Raman modes exhibit downshifting of their frequencies, whereas the B$_{3g}$ band lies near the cutoff limit of the Raman edge filter, hence was not followed and is not discussed further. The T-induced A$_g$ frequency evolution could be followed up to $\sim$550 K, as the Raman spectra become rather featureless beyond this temperature. Such Raman signal disappearance can be attributed both to the reduction of the (integrated) Raman band intensities with increasing temperature [63, 64], as well as to the T-induced carrier concentration increase in SnSe (Fig. 2), which in turn diminishes the collected Raman signal owing to the smaller penetration depth of the incident radiation [65, 66]. Hence, unlike a recent high-temperature Raman investigation [29], we were not able to detect a clear Raman signature of the expected $Pnma \rightarrow Bbmm$ SnSe transition close to 800 K [12–14, 59].

Nevertheless, the isobaric SnSe $Pnma$ Raman mode frequency evolution for both A$_g$ modes as a function of temperature can be fitted to the following polynomial expression (Fig. 3):

$$\omega_i(T) = \omega_{i0} + \left(\frac{\partial \omega_i}{\partial T}\right)_P \Delta T + \left(\frac{\partial^2 \omega_i}{\partial T^2}\right)_P (\Delta T)^2 \tag{4}$$

where ω_{i0} is the mode frequency at ambient conditions, ΔT the temperature difference, and $(\frac{\partial \omega_i}{\partial T})_P$ and $(\frac{\partial^2 \omega_i}{\partial T^2})_P$ the first- and second-order temperature coefficients. The results are tabulated in Table I.

Considering next the value of the volumetric thermal expansion coefficient for SnSe $\alpha_V = 4.19 \cdot 10^{-5}$ K^{-1}, as estimated from the structural data of Ref. 59 within the 300-600 K temperature range of interest, we can in turn calculate the respective isobaric mode Grüneisen parameters γ_i^P [64, 67]:

$$\gamma_i^P = -\frac{1}{\alpha_V \omega_{i0}} \left(\frac{\partial \omega_i}{\partial T}\right)_P \tag{5}$$

with $\gamma_i^P = 40.7$ for the A$_g^3$ mode and $\gamma_i^P = 2.88$ for the A$_g^4$ band, respectively. The magnitude of the obtained A$_g^3$ γ_i^P value is quite large; considering that the A$_g^3$ mode involves atomic motions (almost) parallel to the c-axis (Sn-Se
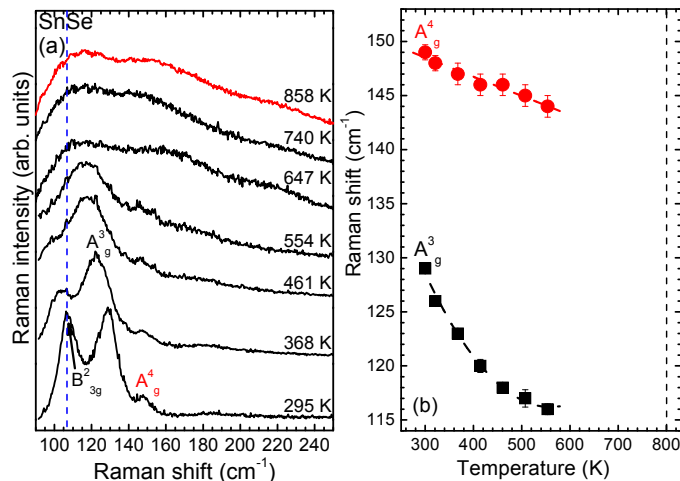
FIG. 3: (a) As-measured Raman spectra of pristine SnSe at various temperatures and ambient pressure, excited with a laser wavelength $\lambda = 473$ nm. The black and red spectra correspond to the *Pnma*- and (the expected) [12–14, 59] high-T *Bbmm*-SnSe phases. The vertical blue dashed line denotes the cutoff limit of the Raman edge filter. (b) Evolution of the SnSe Raman-active mode frequencies as a function of temperature. Lines passing through the data correspond to least square fittings of polynomial functions (eq. 4). The dashed vertical line stands for the expected *Pnma* → *Bbmm* transition [12–14, 59]. The temperature values have been calibrated accordingly [32, 33].

TABLE I: Mode assignment, frequencies, temperature and pressure coefficients, and the isobaric γ_i^P and isothermal γ_i^T mode Grüneisen parameters of the SnSe FIR- and Raman-active vibrations for the *Pnma* and *Bbmm* phases of SnSe, obtained at a reference pressure P_{Ref}. Numbers in parenthesis correspond to the respective calculated values [48].

| Phase	P_{Ref} (GPa)	Assignment	ω_{i0} (cm^{-1})	$\partial\omega_i/\partial T$ (cm^{-1}/K)	$\partial^2\omega_i/\partial T^2$ (cm^{-1}/K^2)	γ_i^P	$\partial\omega_i/\partial P$ (cm^{-1}/GPa)	γ_i^T
Pnma	10^{-4}	B$_{1u}^3$ [48]	157 (159)	-	-	-	4.7 (2.94)	1.07 (0.95)
		A$_g^3$	129 (137.01)	-0.22	-1.9×10^{-4}	40.7	-2.6 (-2.79)	-0.61 (-1.04)
		A$_g^4$	149 (170.74)	-0.018	0	2.88	5.2 (4.4)	1.07 (1.32)
		B$_{2g}^4$	186 (208.57)	-	-	-	2.8 (1.95)	0.47 (0.48)
Bbmm	10	B$_{1g}^2$	152 (164.07)	-	-	-	3 (4.65)	1.97 (2.7)
		A$_g^2$	201 (214.1)	-	-	-	3.3 (3.61)	1.57 (1.61)

intralayer vibration) [48], its sizeable γ_i^P value falls in line with the 'giant' phonon anharmonicity reported for the *Pnma*-SnSe phase along c-axis [18]. Another interesting point is that the A$_g^3$ γ_i^P value is one order of magnitude larger than the respective A$_g^4$ γ_i^P one (the latter arising from vibrations along the long a-axis, i.e. Sn-Se interlayer motions) [48], indicating also the sizeable anisotropy of this material in terms of lattice/phonon anharmonicity, with the intralayer Sn-Se bond anharmonicity being apparently substantially larger compared to the interlayer one [7, 15, 18, 19, 68]. We will return back to this point later below in Sec.III C.

## B. Structural and vibrational response of SnSe under pressure

Several high-pressure structural investigations have established the *Pnma* → *Bbmm* transition in pristine SnSe between 10-15 GPa at ambient temperature [19, 21, 27, 62, 69]. One recent high-pressure XRD study, however, indicated the possibility of a monoclinic modification as the proper choice for indexing the SnSe high-pressure phase [22]. This discrepancy prompted us to conduct a high-pressure XRD study on our SnSe sample in order to elucidate the accurate description of the high-pressure phase.

In Fig. 4 we show examples of Rietveld refinements for the ambient- and high-pressure phases of SnSe, with the respective XRD patterns included in the **Supplement** [48]. It becomes clear that the measured XRD pattern of the high-pressure SnSe phase is accurately reproduced with the established *Bbmm* structural model [19, 21, 27, 62, 69], whereas we could not find the additional Bragg peaks supporting the proposed monoclinic modification [22].

In Fig. 4 we plot the experimentally measured lattice parameters and the respective pressure-volume (P-V) data for both the starting *Pnma* and high-pressure *Bbmm* SnSe phases. The *Pnma* → *Bbmm* transition pressure of our
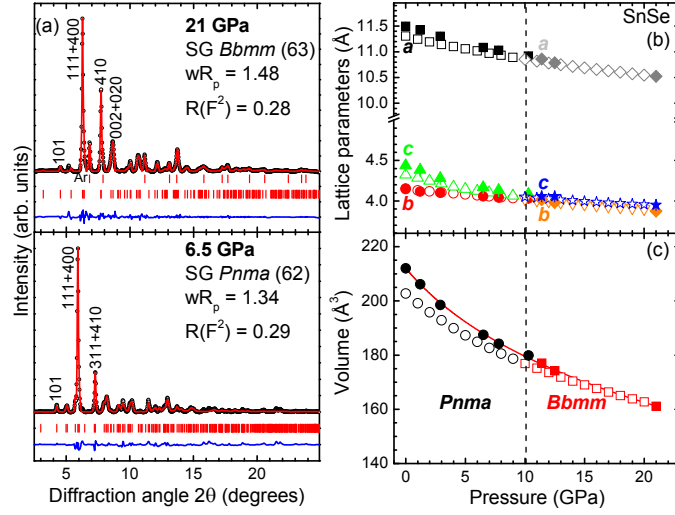
FIG. 4: (a) Examples of Rietveld refinements at 6.5 GPa (SG *Pnma*, bottom) and at 21 GPa (SG *Bbmm*, top) for the measured SnSe XRD diffractograms [48] ($T = 295$ K, $\lambda = 0.29$Å). The black circles and the red solid lines correspond to the measured and the fitted patterns, whereas their difference is depicted as blue lines. Vertical ticks mark Bragg peak positions. (b) Lattice parameters and (c) unit cell-volume as a function of pressure for the ambient-pressure *Pnma* and the high-pressure *Bbmm* phases of SnSe (experimental data: solid symbols, DFT-PBEsol0 calculated data: open symbols). The red solid line running through the experimental P-V data represents the fitted Davis-Gordon EoS form [70]. The vertical dashed line marks the onset of the $Pnma \rightarrow Bbmm$ structural transition. Error bars lie within the symbols.
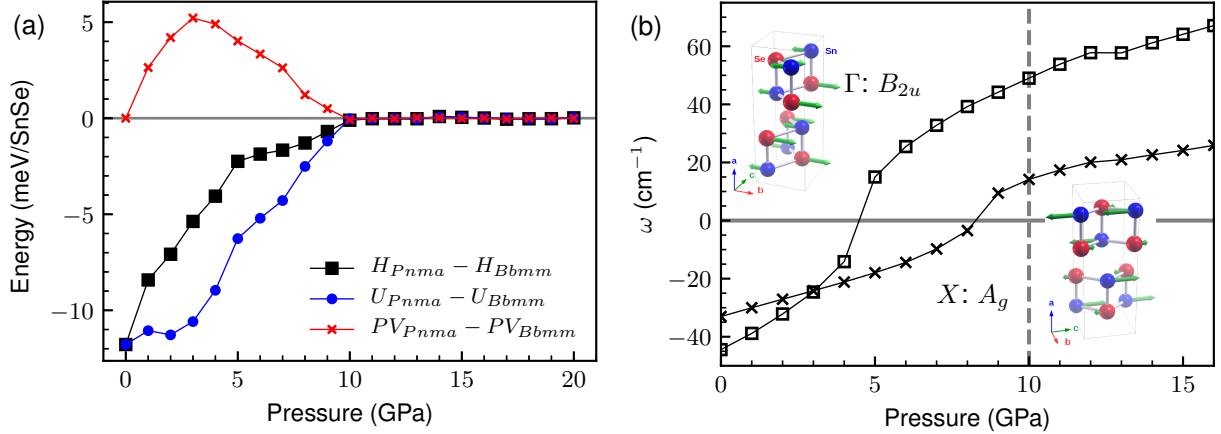
FIG. 5: (a) Calculated (DFT-PBEsol0) pressure dependence of the enthalpy difference $\Delta H = H_{Pnma}$-H_{Bbmm} between the *Pnma*-SnSe and *Bbmm*-SnSe phases. The individual enthalpy differences from the internal energy (U) and volume (PV) dependence are also shown and denoted by blue circles and red crosses, respectively. All values are given for $T = 0$ K and phonon effects are neglected. (b) Pressure dependence of the Γ-B_{2u} and X-A_g phonon frequencies, which are responsible for the instability of *Bbmm*-SnSe phase. The negative abscissa denotes imaginary frequencies. The corresponding ambient-pressure eigenvectors for the Γ-B_{2u} and X-A_g modes are also shown. Lines are guides for the eye.

SnSe sample is close to 10 GPa, in excellent agreement with previous reports [19, 21, 27, 62, 69]. In addition, the $Pnma \rightarrow Bbmm$ structural transition can be classified as a second-order transition, i.e. without any apparent volume discontinuity at the transition point. For this reason, the *Pnma* and *Bbmm* P-V data can be described by the same equation of state (EoS), with the Davis-Gordon EoS form [70] constituting the best choice [21]. The respective volumes, bulk moduli, and bulk moduli derivatives of the SnSe *Pnma* and *Bbmm* phases are provided in Table II, alongside literature values [19, 21, 22, 27, 69].

In order to verify our experimental structural observations, we have calculated the enthalpies $[H(P) = U + PV]$ for the starting *Pnma* and the high-pressure *Bbmm* SnSe modifications (Fig. 5). At zero pressure, *Pnma*-SnSe lies 12 meV/SnSe lower in enthalpy compared to the *Bbmm*-SnSe phase. With increasing pressure, the enthalpy difference $\Delta H = H_{Pnma}$-H_{Bbmm} decreases and becomes zero close to 10 GPa, i.e. the *Pnma* and *Bbmm* enthalpies

TABLE II: Volume V, bulk modulus B, and its pressure derivative B' for the ambient-pressure $Pnma$ and the high-pressure $Bbmm$ phases of SnSe at a reference pressure point P_{Ref}, as obtained by a Davis-Gordon EoS form[70] fit to our experimental and computed P-V data. The term 'fixed' refers to parameters not allowed to vary during the fitting. Relevant results from the literature are also listed for direct comparison. Abbreviations are defined as PTM: pressure transmitting medium, N/A: not available, M/E/W: Methanol-ethanol-water 16:3:1 mixture, GGA: Generalized Gradient Approximation, D2: Dispersion correction.

| SnSe phase	Method	PTM	P_{Ref} (GPa)	V Å^3	B (GPa)	B' (GPa)
$Pnma$	XRD	Argon	10^{-4}	212.03 (fixed)	40(2)	5.3(7)
	DFT-PBEsol0	N/A	10^{-4}	202.69	51.2(7)	5.6(3)
	XRD[28]	N/A	10^{-4}	N/A	50.3(5)	6.3
	XRD[21]	Helium	10^{-4}	212.23 (fixed)	31.1(2)	8.04(10)
	XRD[22]	M/E/W	10^{-4}	210	39.8	4.31
	XRD[27]	Daphne oil	10^{-4}	214.4	39.8	4.31
	DFT-GGA[69]	N/A	10^{-4}	272.96	31.48	N/A
	DFT-GGA[73]	N/A	10^{-4}	218.86	34.2	4 (fixed)
	DFT-GGA+D2[26]	N/A	10^{-4}	211.87	34.45	7.38
$Bbmm$	XRD	Argon	10.4	177.05 (fixed)	80(2)	5.3(7)
	DFT-PBEsol0	N/A	10	176.86	95.2(7)	5.6(3)
	XRD[21]	Helium	10.5	176	31.1(2)	8.04(10)
	XRD[27]	Daphne oil	20	198	55.4	4.55
	DFT-GGA[69]	N/A	10^{-4}	240	40.9	N/A

become (within error) identical. Such behavior is characteristic for a second-order transition, and the calculated $Pnma \rightarrow Bbmm$ transition pressure is in excellent agreement with both the experimentally determined transition pressure value (Fig. 4), as well as with previous enthalpy calculations [19, 27, 69]. Closer inspection of the individual enthalpy contributions reveals two distinct slopes in the energetics of the pressure-induced $Pnma \rightarrow Bbmm$ phase transition. In particular, the significant decrease of $\mid \Delta H \mid$ within 0–5 GPa, is driven by the $P\Delta V$ term up to 3 GPa and the difference in cell volumes, with $V_{Pnma}(P_i) > V_{Bbmm}(P_i)$, whereas $\mid \Delta H \mid$ is dominated by changes in the internal energy U from 3 to 5 GPa. Within the 5-10 GPa pressure range, the variation of $\mid \Delta H \mid$ is significantly reduced, as the $P\Delta V$ and ΔU terms exhibit similar magnitudes and partially cancel each other out. Our results clearly show that the enthalpy difference between the $Pnma$ and $Bbmm$ phases of SnSe can be significantly reduced by the application of pressures below the critical transition pressure of 10 GPa. This small energetic difference between the $Pnma$ and $Bbmm$ phases of SnSe may then effectively lower the critical transition temperature, thus allowing for the investigation of the $Bbmm$-SnSe thermoelectric properties below $T = 800$ K [10, 19, 25].

Interestingly, the calculation of the $Bbmm$ phonons reveals two imaginary TO vibrational frequencies at the center Γ (0, 0, 0) and at the X symmetry point (0.5, 0, 0) of the $Bbmm$ Brillouin zone at ambient pressure, indicating the instability of the $Bbmm$ phase (Fig. 5), consistent with earlier calculations [10, 11, 19, 71]. The calculated ambient-pressure phonon eigenvectors indicate that these imaginary IR-active Γ-B$_{2u}$ and X-A$_g$ modes correspond to opposing Sn-Se displacements parallel to the $Bbmm$ b- and c-axis, respectively (Fig. 5), where the latter X-A$_g$ vibration represents the primary distortion mode of the second-order/displacive $Pnma \rightarrow Bbmm$ transition in SnSe [10, 11, 17, 59].

Increasing pressure results in a frequency upshift for both vibrations due to the contraction of the respective b- and c-axis (Fig. 4). The increased pressure sampling of these modes shows, to our knowledge for the fist time, that the imaginary B$_{2u}$ and the A$_g$ modes become 'stable', i.e. adopt positive frequency values at 5 GPa and 9 GPa, respectively (Fig. 5), just 1 GPa below the critical $Pnma \rightarrow Bbmm$ transition pressure. Thus, the pressure dependence of the dynamical instability of $Bbmm$-SnSe is apparently more intricate than previously reported, as the stabilization of $Bbmm$-SnSe requires the simultaneous application of compressive stress along the respective b- (B$_{2u}$ mode) and c-axis (A$_g$ mode).

Finally, in Fig. 4 we plot the calculated structural parameters for both phases alongside their experimental counterparts. Generally we can observe a very good agreement between the two data sets, with the exception of the $Pnma$ volume. The latter is underestimated in our calculations with respect to the experimental values, a well-known effect within the DFT approximation [72]. The respective calculated volumes, bulk moduli, and bulk moduli derivatives for the SnSe $Pnma$ and $Bbmm$ phases are listed in Table II.

Having established the structure of the high-pressure SnSe phase, we turn now to the high-pressure vibrational properties of SnSe at ambient temperature. In Fig. 6 we show selected Raman spectra at various pressures. At ambient conditions, we can clearly observe the three B$_{3g}^2$, A$_g^3$, and A$_g^4$ Raman features of the SnSe $Pnma$ phase (eq. 2) as in our high-T study (Fig. 3). Upon increasing pressure, the A$_g^3$ mode exhibits a pressure-induced frequency
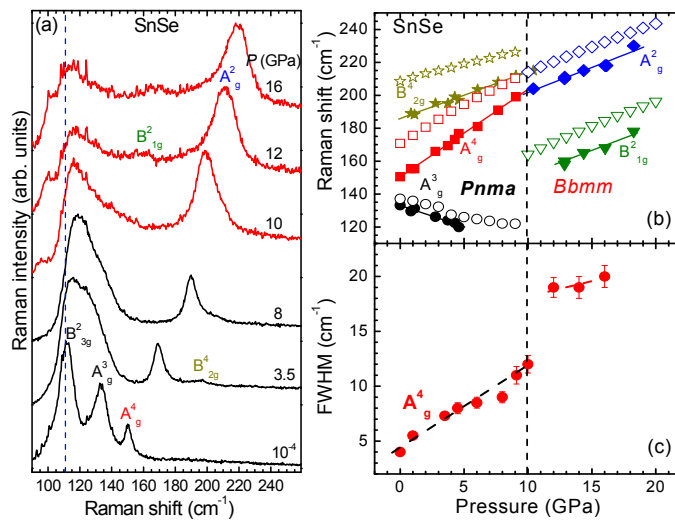
FIG. 6: (a) Raman spectra of pristine SnSe at selected pressures ($T = 295$ K, $\lambda = 633$ nm). The black and red spectra correspond to the *Pnma*- and the high-pressure *Bbmm*-SnSe phases, respectively. The vertical dashed blue line denotes the cutoff limit of the Raman edge filter. The high-pressure Raman spectra of SnSe collected with $\lambda = 473$ nm yielded identical results as the $\lambda = 633$ nm experimental run. (b) Evolution of Raman mode frequencies as a function of pressure. The closed and open symbols correspond to experimental and DFT-PBEsol0 data, respectively. The vertical dashed line represents the onset of the *Pnma* $\rightarrow$ *Bbmm* structural transition. Error bars lie within the symbols. (c) Pressure-induced behavior of the A_g^4 *Pnma* Raman-active mode's full width at half maximum (FWHM), as determined by Lorentzian fittings on the experimental data.

softening and merges with the adjacent B_{3g}^2 band, hence was followed only up to ∼5 GPa; the detection of the A_g^3 band beyond that pressure was not possible due to the cutoff limit of the Raman filter. Nevertheless, since this mode is associated (mainly) with Sn-Se motions along the *c*-axis [48], its mode frequency drop against pressure directly indicates a decrease of the respective force constant. Considering the interatomic parameter evolution of the SnSe *Pnma* phase, such explanation can be rationalized from e.g. the pressure-induced expansion of specific Sn-Se bond lengths along the *c*-axis (termed as A_1 in Ref. 21) across the *Pnma* $\rightarrow$ *Bbmm* structural transformation.

On the other hand, the A_g^4 band displays the expected frequency upshift upon compression (Fig. 6). This vibration results from Sn-Se motions along the *a*-axis, i.e. is dependent on the Sn-Se interlayer distance [48], which decreases as a function of pressure (Fig. 4). Close inspection of the A_g^4 Raman mode frequency evolution reveals a subtle change in its pressure dependence close to 10 GPa. In addition, the width of this band exhibits an abrupt increase around this pressure value (Fig. 6). Considering that the *Pnma* $\rightarrow$ *Bbmm* structural transition takes place at this pressure (Fig. 4), we interpret both of these effects as the Raman fingerprint of the pressure-induced *Pnma* $\rightarrow$ *Bbmm* transition in SnSe. Similar observations from high-pressure Raman spectroscopic experiments on SnSe nanosheets were reported recently [62]. Finally, we mention the detection of the low-intensity *Pnma* B_{2g}^4 Raman mode upon moderate compression; the latter vibration exhibited 'normal' blueshift of its frequency under pressure, whereas we were not able to observe this band beyond the *Pnma* $\rightarrow$ *Bbmm* transition pressure (Fig. 6).

Upon entering the pressure stability regime of the *Bbmm*-SnSe phase, we could observe two out of the six expected Raman-active modes (eq. 3); both of them upshift in frequency upon compression (Fig. 6). Our DFT-PBEsol0 calculated Raman mode frequencies are also presented in Fig. 6; despite the numerical discrepancies in the Raman mode frequency values for both the *Pnma*- and the *Bbmm*-SnSe phases resulting from the approximations within DFT [72], the pressure dependencies of the Raman-active bands are consistently reproduced (Fig. 6 and Table I).

Turning now to the analysis of the measured Raman data, the Raman mode frequency evolution as a function of pressure can be modelled with the following expression:

$$\omega_i(P) = \omega_{i0} + \left(\frac{\partial \omega_i}{\partial P}\right)_T \Delta P \qquad (6)$$

where ω_{i0} is the mode frequency at ambient conditions, ΔP the pressure difference, and $(\frac{\partial \omega_i}{\partial P})_T$ the first-order pressure coefficient. We note that in our case, we did not need to include any higher-order pressure coefficient terms for fitting the ω-P data (Fig. 6). The results are listed in Table I. Considering the bulk moduli values for the *Pnma* and *Bbmm*

phases, as determined from our high-pressure XRD investigation (Table II), we can derive the respective isothermal mode Grüneisen parameters γ_i^T [64, 67]:

$$\gamma_i^T = \frac{B}{\omega_{i0}} \left(\frac{\partial \omega_i}{\partial P}\right)_T \tag{7}$$

with the respective γ_i^T values tabulated in Table I. Having this information at hand, we can now evaluate the respective mode-specific phonon anharmonicity of the detected SnSe $Pnma$ Raman-active modes.

C. Phonon anharmonicity in the SnSe $Pnma$ phase

As we mentioned in the **Introduction**, one of the most critical factors in determining the thermoelectric efficiency of SnSe is the lattice thermal conductivity κ_{lat}. The latter has been shown to be strongly dependent on phonon scattering processes, involving phonon-phonon interactions and relevant phonon anharmonic effects [7, 9–11, 15–19]. Even though for an accurate description of anharmonic effects in either the $Pnma$ or $Bbmm$ phases of SnSe one should take into account the complete phonon density of states, an elementary understanding of SnSe phonon anharmonicity can be acquired from our high-T and high-P Raman measurements. In particular, the isobaric temperature dependence of Raman-active mode frequencies can be approximated by the following expression [64, 67, 74]:

$$\left(\frac{\partial \omega_i}{\partial T}\right)_P = -B_0 \alpha_V \times \left(\frac{\partial \omega_i}{\partial P}\right)_T + \left(\frac{\partial \omega_i}{\partial T}\right)_V \tag{8}$$

In this equation, the $-B_0\alpha_V \times (\frac{\partial \omega_i}{\partial P})_T$ term stands for the volumetric thermal expansion contribution (implicit term), whereas the $(\frac{\partial \omega_i}{\partial T})_V$ part describes the anharmonic phonon interactions (explicit term) to the mode-specific temperature dependence. Strictly speaking, this expression is valid only for isotropic crystals [64, 74]; nevertheless, we are using this relationship as a first approximation in gaining a qualitative understanding of the phonon anharmonicity in SnSe. Consequently, by using the determined temperature $(\frac{\partial \omega_i}{\partial T})_P$ and pressure $(\frac{\partial \omega_i}{\partial P})_T$ coefficients (Table I), as well as the $\alpha_V = 4.19\cdot10^{-5}$ (K^{-1}) [59] and $B_0 = 40$ GPa (Table II) values, we can in turn determine the implicit and explicit contributions to each of the A_g^3 and A_g^4 $Pnma$-SnSe modes. In particular, we calculate $-B_0\alpha_V \times (\frac{\partial \omega_i}{\partial P})_T = 0.0044$ cm^{-1}K^{-1} and $(\frac{\partial \omega_i}{\partial T})_V = -0.2244$ cm^{-1}K^{-1} for the A_g^3, and $-B_0\alpha_V \times (\frac{\partial \omega_i}{\partial P})_T = -0.0087$ cm^{-1}K^{-1} and $(\frac{\partial \omega_i}{\partial T})_V = -0.0093$ cm^{-1}K^{-1} for the A_g^4 mode. The results are listed in Table III.

Comparison of the estimated explicit and implicit factors of eq. 8 between the two $Pnma$-SnSe Raman-active modes shows that (a) the anharmonic (explicit) component of the A_g^3 band is the dominant factor in determining the T-dependence of this vibration, (b) the implicit and explicit contributions to the A_g^4 mode are of almost equal strength, (c) the anharmonic component of the A_g^3 mode is one order of magnitude larger than the corresponding A_g^4 one (as already indicated by the one order of magnitude larger γ_i^P values, Table I), and (d) the implicit contributions of the A_g^3 and the A_g^4 modes exhibit *opposite* signs, owing to the pressure-induced softening of the A_g^3 vibration (Fig. 6 and Table I).

A deeper understanding of the anharmonic phonon processes can be gained by considering a more generalized expression for the Raman-active mode temperature dependence [64, 75]:

$$\Delta \omega_i(T) = \Delta \omega_E(T) + \Delta \omega_A(T) \tag{9}$$

where $\Delta \omega_E(T)$ stands for the implicit and $\Delta \omega_A(T)$ for the explicit contributions to the frequency dependence. $\Delta \omega_E(T)$ equals to [64, 75]:

$$\Delta \omega_E(T) = \omega_{i0h} \left[\exp\left(-n \int_{0\ K}^{T} \gamma_i^T \alpha_V dT\right) - 1\right] \tag{10}$$

with ω_{i0h} representing the harmonic mode frequency at 0 K, n denoting the degeneracy of the Raman-active vibration ($n = 1$ for the A_g modes examined here), and α_V the volumetric thermal expansion coefficient of SnSe. The temperature dependence of α_V within the 0-600 K temperature range can be estimated from the data of Ref. 59:

$$\alpha_V(T) = \frac{8 \times 10^{-6} \times T + 0.0059}{V_0} K^{-1} \tag{11}$$

TABLE III: Calculated implicit and explicit terms from eq. 8, as well as the estimated A and B fitting parameters of eq. 12 for the two $Pnma$-SnSe A_g Raman-active modes. The numbers in parenthesis are results from Ref. 29.

Mode	$-B_0\alpha_V \times (\frac{\partial\omega_i}{\partial P})_T$ (cm^{-1}K^{-1})	$(\frac{\partial\omega_i}{\partial T})_V$ (cm^{-1}K^{-1})	ω_{i0h} (cm^{-1}) [29]	A (cm^{-1})	B (cm^{-1})
A_g^3	0.0044	-0.2244	143.6	-3.31±1 (-1.252)	0.03±1 (-0.006)
A_g^4	-0.0087	-0.0093	154	-0.79±5	0.02±1

with $V_0 = 210.22$ Å^3 the (extrapolated) SnSe volume at 0 K, and T the temperature in Kelvin. Since we do not know the temperature dependence of the isothermal mode Grüneisen parameter γ_i^T, we assume for the sake of simplicity that γ_i^T is temperature independent. Furthermore, $\Delta\omega_A(T)$ can be expressed by the following equation [75]:

$$\Delta\omega_A(T) = A\left[1 + \frac{2}{e^x - 1}\right] + B\left[1 + \frac{3}{e^y - 1} + \frac{3}{(e^y - 1)^2}\right] \quad (12)$$

with $x = \hbar\omega_{i0h}/2k_BT$, $y = \hbar\omega_{i0h}/3k_BT$, where $\hbar$ is Planck's constant divided by 2π, k_B is Boltzmann's constant, and A and B stand for anharmonic constants acting as fitting parameters and indicating the strength of the three-(cubic) and four-phonon (quartic) processes, respectively, i.e. the decay of one optical Γ phonon into two or three phonons at different points of the Brillouin zone by obeying energy and momentum conservation [76].
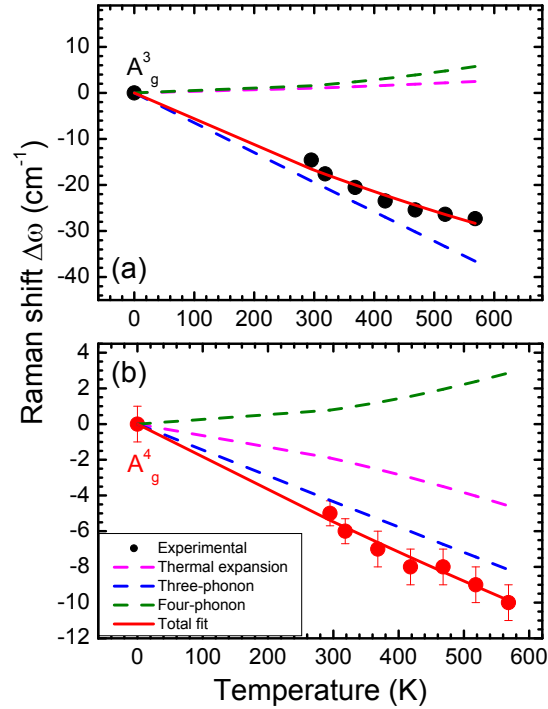
FIG. 7: Temperature-induced frequency shifts $\Delta\omega$ of the $Pnma$-SnSe Raman-active modes (a) A_g^3 and (b) A_g^4 at ambient pressure. The closed symbols depict the experimental data points, whereas the solid red lines stand for the total fittings including the individual contributions of thermal expansion effects (dashed magenta lines), and three-phonon (dashed blue lines) and four-phonon (dashed green lines) processes (see text for more details). The ω_{i0h} values at 0 K are taken from Ref. 29.

Combining eqs. 9-12, Fig. 7 displays the respective fittings of the $Pnma$-SnSe A_g Raman mode frequencies against temperature. We can readily observe that (a) the three-phonon term dominates the behavior for both modes, (b) the thermal expansion term for the A_g^3 mode is negligible, whereas the respective contribution for the A_g^4 mode is significantly larger compared to that of A_g^3 and comparable with the three-phonon term, and (c) the four-phonon process term exhibits a *positive* temperature dependence above 300-350 K for both A_g modes, with a more noticeable influence in the A_g^4 mode, stemming from the positive B anharmonic constants (Table III) and possibly implying up-conversion decay channels beyond that temperature [77]. Since both of the experimental A_g Raman mode frequencies decrease upon heating, the latter behavior implies that phonon anharmonicity is mainly dictated by three-phonon

processes, which show negative temperature dependencies for both modes and cancel the marginally positive four-phonon contributions (Fig. 7 and Table III).

We should mention, however, that a similar analysis has recently appeared in the literature, covering a more extensive temperature range (2-800 K) [29]. In that study, the authors obtained similar results as the ones presented here, i.e. that the phonon anharmonicity of the Raman-active modes is dictated mainly by three-phonon processes. Nevertheless, certain discrepancies can be observed in the two investigations, e.g. the thermal expansion term for the A_g^3 mode in Ref. 29 is shown to exhibit negative temperature dependence, unlike the negligible temperature dependence found here (Fig. 7). The reason for this discrepancy is derived from the different parameters used for the evaluation of this specific contribution, as Liu *et al.* [29] adopted the *average* thermodynamic Grüneisen parameter of SnSe for estimating the thermal volume expansion term in eq. 10, whereas here we employed the mode-specific isothermal Grüneisen parameters γ_i^T for the evaluation of this contribution individually for each Raman-active mode (Table I). The latter is also reflected in the numerical differences of the thermal volume expansion terms in the two works. Considering relevant works from the literature on other materials [64, 67, 77, 78], it appears that the proper modelling of the thermal expansion contribution $\Delta\omega_E(T)$ in eq. 9 requires mode-specific Grüneisen parameters. Finally, the evaluated A and B anharmonic constant values exhibit notable numerical differences (Table III); this disagreement can be easily rationalized by considering the aforementioned different thermal expansion contributions $\Delta\omega_E(T)$ in the two works, which can in turn result in different estimates for the derived A and B fitting parameters due to the close interrelation between the $\Delta\omega_E(T)$ and $\Delta\omega_A(T)$ terms (eq. 9).

D.   Electronic and optical properties of SnSe as a function of pressure

Another key ingredient for determining the thermoelectric performance of a material is the electrical conductivity (eq. 1). For this reason, we have also examined the effect of pressure on the electronic properties of SnSe. In Fig. 8 we show the calculated electronic band structure and density of states (DOS) for the *Pnma*- and *Bbmm*-SnSe phases at selected pressures. At ambient conditions, SnSe is an indirect band gap semiconductor, exhibiting multiple valence band maxima (VBM) with similar energies along the *Z*-Γ-*Y* paths, while the conduction band minimum (CBM) at the Γ-point is accompanied by secondary CBMs along the *Z*-Γ-*Y* direction (Fig. 8). The atom-projected DOS reveals that the VBM are primarily composed of Se-*p* states, whereas the CBMs consist mainly of unoccupied Sn states. At ambient pressure, the calculated *Pnma*-SnSe (*Bbmm*) band gaps are $E_g = 1.14$ eV (0.64 eV). Application of external hydrostatic pressure leads to the progressive band gap reduction, and at 9 GPa SnSe exhibits semi-metallic behavior (Fig. 8). The semi-metallic character increases upon further compression and leads to the divergence of the dielectric constant along the *b*-axis, as we discuss in the next paragraphs. Overall, the calculated electronic band structure and its pressure-induced evolution at the PBEsol0 level of theory for SnSe agrees very well with previous experimental and theoretical investigations [7, 9, 10, 19, 22–24, 26, 27, 59, 73, 79–82].

Additional insights on the mechanism of the pressure-induced $Pnma \rightarrow Bbmm$ transition can be provided from the calculated IR reflectance spectra of the *Pnma*- and *Bbmm*-SnSe phases presented in the **Supplement** [48]. For these spectra we have evaluated the respective dielectric constants $(\varepsilon_\infty)_{ll}$ and the Born effective dynamic charges $(e_T^*)_{ll}$ for each crystallographic direction l at various pressures at the DFT-PBEsol0 level of theory, using the coupled perturbed Kohn-Sham CPKS method [52–55]. The determined $(e_T^*)_{ll}$ values can be used in turn to determine the frequency difference between the respective transverse optical (TO) and longitudinal optical (LO) modes, i.e. the LO-TO splitting along each crystallographic direction for the orthorhombic *Pnma*- and *Bbmm*-SnSe phases from [83]:

$$\omega_{LO}^2(l) - \omega_{TO}^2(l) = \frac{16\pi(e_T^*)_{ll}^2}{(\varepsilon_\infty)_{ll}V\mu} \tag{13}$$

where ε_∞ is the high-frequency (electronic) dielectric constant, V the volume, and μ the reduced mass of Sn and Se.

We discuss first the obtained LO-TO splittings for the most intense IR-active vibrations along the different crystallographic orientations across the pressure-induced $Pnma \rightarrow Bbmm$ transition. The results are plotted in Fig. 9(a). We can observe that the LO-TO splitting marginally decreases along the *Pnma a*-axis, whereas a noticeable increase occurs along the *b*- and *c*-directions upon compression, as in several wurtzite-type binary semiconductors [83–85]. Upon adopting the *Bbmm* phase after 10 GPa, however, the trend in the LO-TO splitting behavior along the *b*-axis shows a *negative* pressure dependence, the *c*-axis LO-TO splitting plateaus, whereas the *a*-axis LO-TO splitting appears unaffected (Fig. 9).

Turning now to the ε_∞ values, the results are plotted in Fig. 9(b). We can readily observe that the *Pnma*-SnSe ε_∞ values increase with increasing pressure in every direction, owing to the progressive band gap closure upon compression (Fig. 8). After the adoption of the *Bbmm*-SnSe phase at 10 GPa, the ε_∞ along the *b*-axis exhibits a remarkable superlinear behavior, whereas the *Bbmm*-SnSe *a*- and *c*-axis ε_∞ do not show any appreciable variations.
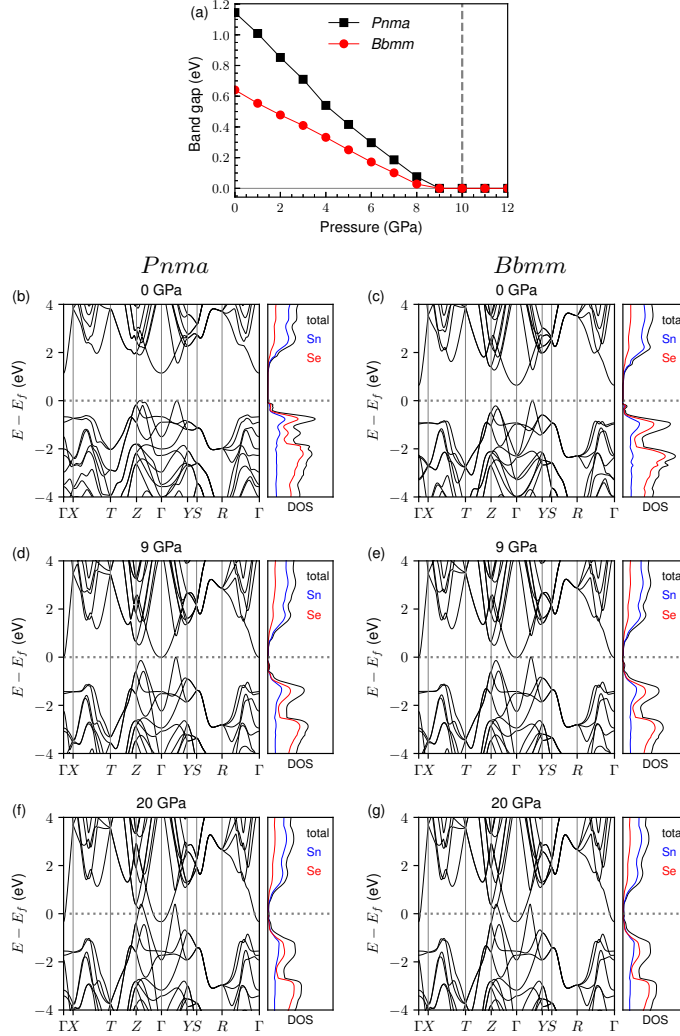
FIG. 8: (a) Calculated pressure dependence of the bulk electronic band gap E_g for the $Pnma$ (black squares) and $Bbmm$ (red circles) SnSe phases. The vertical dashed gray line marks the (calculated) $Pnma \rightarrow Bbmm$ structural transition, as determined from our enthalpy calculations (Fig. 5), whereas the lines passing through the data serve as guides for the eye. (b-g) Calculated band structures and atom-projected density of states (DOS) at the DFT-PBEsol0 level for the ambient-pressure $Pnma$-SnSe and the high-pressure $Bbmm$-SnSe modification at selected pressures.

This observation implies that the semi-metallic character of SnSe is strongly direction-dependent and can be mainly induced by the compression of the orthorhombic b-axis.

Regarding finally the pressure-induced evolution of the Born effective charge, in Fig. 9(c) we plot the normalized e_T^* values for the three different $Pnma$ and $Bbmm$ crystallographic directions. Interestingly, we can observe that the effective charge *increases* along all crystal axes upon compression for both the $Pnma$- and $Bbmm$-SnSe phases, implying a pressure-induced effective charge transfer from the Sn^{2+} cations towards the Se^{2-}. Considering all the factors entering the calculation of e_T^* (eq. 13), it appears that the most prominent contribution stems from ε_∞ which increases also upon compression [Fig. 9(b)].

Remarkably, such pressure-induced e_T^* enhancement is highly unusual for materials, as it is contrasting the generic trend of several binary semiconductors showing negative or (almost) zero e_T^* pressure dependencies [84–86]. The only other known example of a compound exhibiting pressure-induced e_T^* increase is 3C-SiC [83]. A recent work associated the pressure dependence of e_T^* in these binary systems with the ambient-pressure interatomic bond ionicity f_i [85], the latter being a physical parameter developed by Philips and Van Vechten reflecting the interatomic electronegativity difference [87]. Without going into many details here, the SnSe bond ionicity at ambient pressure was found to be $f_i \simeq 0.7$ [88, 89], a value which should 'cause' a negative pressure dependence of SnSe-e_T^* according to Reparaz *et al.* [85], which is clearly not the case. Hence, both the origin of the e_T^* pressure dependence, as well as a potential
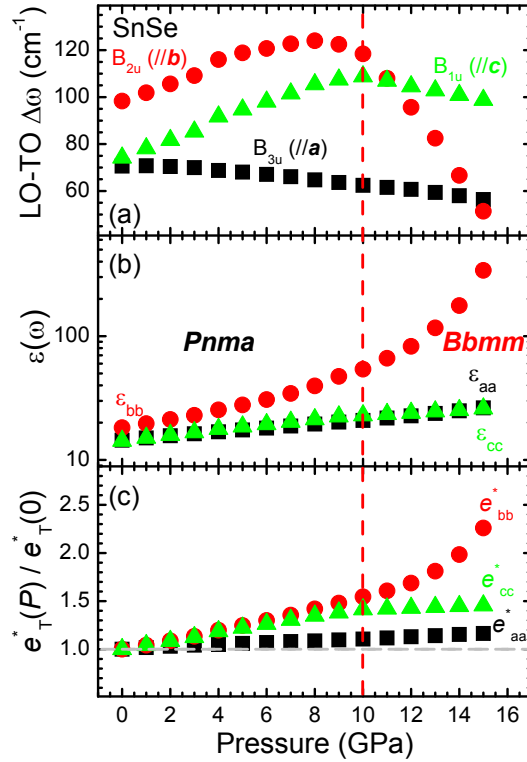
FIG. 9: Pressure-induced evolution of the direction-dependent (a) LO-TO splitting, (b) ε_∞, and (c) the Born effective charge e_T^*, as determined from the calculated FIR reflectance spectra for the *Pnma*- and the high-pressure *Bbmm*-SnSe phases. The ε_∞ values are plotted in a logarithmic scale to facilitate comparison. The vertical dashed line represents the onset of the *Pnma* → *Bbmm* structural transition.

link to the interatomic bond ionicity/polarity/ electronegativity difference should be revisited.

IV. CONCLUSIONS

We have investigated the optical and vibrational properties of the binary semiconductor SnSe as a function of temperature and pressure by means of experimental and *ab initio* methods. Our high-T reflectance investigations have successfully reproduced the progressive enhancement of free carrier concentration upon approaching the high-temperature *Bbmm* phase [7]; at the same time, a relevant contribution of free electrons to the thermal conductivity could be discarded due to the very high scattering rate deduced from the far-infrared reflectance spectra. Furthermore, the Raman fingerprint of the pressure-induced *Pnma* → *Bbmm* transition has been identified for bulk SnSe close to 10 GPa at ambient temperature, in excellent agreement with our high-pressure XRD experiments and first-principles calculations. The reported semiconductor→semi-metal transition accompanying the *Pnma* → *Bbmm* structural transformation in SnSe [7, 9, 10, 19, 22–24, 26, 27, 59, 73, 79–82] has been successfully reproduced from our first-principles band structure calculations.

Combination of our high-temperature (at ambient pressure) and high-pressure (at ambient temperature) Raman measurements allowed for the determination of the respective isobaric and isothermal mode-specific Grüneisen parameters for the first time in bulk SnSe, key parameters for modelling the thermoelectric properties of this system (especially) at high temperatures where the optical modes can become relevant for thermal conductivity [7, 19, 68, 79]. In addition, modelling of the temperature dependence of the detected Raman-active mode frequencies using the well-established thermal expansion and anharmonic contributions has revealed that three-phonon anharmonic processes dominate the T-induced Raman mode frequency evolution, similar to a very recent study [29].

Finally, we calculated the evolution of the SnSe FIR reflectance as a function of pressure across the *Pnma* → *Bbmm* structural transition. Out of these investigations, we acquired the pressure dependencies of relevant optical, vibrational, and electronic parameters such as the LO-TO mode splittings, the high-frequency dielectric constants ε_∞, and the Born effective charges e_T^*. The most remarkable finding is the pressure-induced *enhancement* of e_T^* for

both the *Pnma*- and *Bbmm*-SnSe modifications, a rather unique feature among binary materials [84–86] with the notable exception of 3C-SiC [83]. Interestingly, the recently proposed link between the pressure dependence of e_T^* and the interatomic bond ionicity [85] is not applicable for SnSe. Consequently, the origin behind the positive e_T^* pressure dependence of both SnSe and 3C-SiC [83], two seemingly unrelated materials, remains an interesting open question.

CONFLICTS OF INTEREST

There are no conflicts to declare.

ACKNOWLEDGEMENTS

[1] L. E. Bell, Science **321**, 1457 (2008).
[2] K. Biswas, J. Q. He, I. D. Blum, C. I. Wu, T. P. Hogan, D. N. Seidman, V. P. Dravid, and M. G. Kanatzidis, Nature **489**, 414 (2012).
[3] C. Chang, G. Tan, J. He, M. G. Kanatzidis, and L.-D. Zhao, Chem. Mater. **30**, 7355 (2018).
[4] W. Shi, M. Gao, J. Wei, J. Gao, C. Fan, E. Ashalley, H. Li, and Z. Wang, Adv. Sci. **5**, 1700602 (2018).
[5] G. Tan, L.-D. Zhao, and M. G. Kanatzidis, Chem. Rev. **116**, 12123 (2016).
[6] A. Kokalj, Comp. Mater. Sci. **28**, 155 (2003).
[7] L.-D. Zhao, S.-H. Lo, Y. Zhang, H. Sun, G. Tan, C. Uher, C. Wolverton, V. P. Dravid, and M. G. Kanatzidis, Nature **508**, 373 (2014).
[8] J. Wu, Y. B. Chen, J. Q. Wu, and K. Hippalgaonkar, Adv. Electron. Mater. **4**, 1800248 (2018).
[9] R. Guo, X. Wang, Y. Kuang, and B. Huang, Phys. Rev. B **92**, 115202 (2015).
[10] A. Dewandre, O. Hellman, S. Bhattacharya, A. H. Romero, G. K. H. Madsen, and M. J. Verstraete, Phys. Rev. Lett. **117**, 276601 (2016).
[11] J. M. Skelton, L. A. Burton, S. C. Parker, A. Walsh, C.-E. Kim, A. Soon, J. Buckeridge, A. A. Sokol, C. R. A. Catlow, A. Togo, and I. Tanaka, Phys. Rev. Lett. **117**, 075502 (2016).
[12] H. G. von Schnering and H. Wiedemeier, Z. Kristallogr. **156**, 143 (1981).
[13] M. Sist, J. Zhang, and B. B. Iversen, Acta Cryst. B **72**, 310 (2016).
[14] T. Chattopadhyay, J. Pannetier, and H. G. von Schnering, J. Phys. Chem. Sol. **47**, 879 (1986).
[15] D. Bansal, J. Hong, C. W. Li, A. F. May, W. Porter, M. Y. Hu, D. L. Abernathy, and O. Delaire, Phys. Rev. B **94**, 054307 (2016).
[16] J. Carrete, N. Mingo, and S. Curtarolo, Appl. Phys. Lett. **105**, 101907 (2014).
[17] T. Chatterji, U. D. Wdowik, G. Jaglob, S. Rolsa, and F. R. Wagner, Phys. Lett. A **382**, 1937 (2018).
[18] C. W. Li, J. Hong, A. F. May, D. Bansal, S. Chi, T. Hong, G. Ehlers, and O. Delaire, Nature Phys. **11**, 1063 (2015).
[19] H. Yu, S. Dai, and Y. Chen, Sci. Rep. **6**, 26193 (2016).
[20] Y. Li, B. He, J. P. Heremans, and J.-C. Zhao, J. Alloys Compd. **669**, 224 (2016).
[21] I. Loa, R. J. Husband, R. A. Downie, S. R. Popuri, and J.-W. G. Bos, J. Phys. Cond. Matt. **27**, 072202 (2015).
[22] J. Yan, F. Ke, C. Liu, L. Wang, Q. Wang, J. Zhang, G. Li, Y. Han, Y. Ma, and C. Gao, Phys. Chem. Chem. Phys. **18**, 5012 (2016).
[23] D. D. Cuong, S. H. Rhim, J.-H. Lee, and S. C. Hong, AIP Advances **5**, 117147 (2015).
[24] M. S. Gusmao, C. Mota, A. Ghosh, and H. O. Frota, Comput. Mater. Sci. **152**, 243 (2018).
[25] Y. Zhang, S. Hao, L.-D. Zhao, C. Wolverton, and Z. Zeng, J. Mater. Chem. A **4**, 12073 (2016).
[26] K. Nguyen-Cong, J. M. Gonzalez, B. A. Steele, and I. I. Oleynik, J. Phys. Chem. C **122**, 18274 (2018).
[27] X. Chen, P. Lu, X. Wang, Y. Zhou, C. An, Y. Zhou, C. Xian, H. Gao, Z. Guo, C. Park, B. Hou, K. Peng, X. Zhou, J. Sun, Y. Xiong, Z. Yang, D. Xing, and Y. Zhang, Phys. Rev. B **96**, 165123 (2017).
[28] T. Chattopadhyay, A. Werner, H. G. von Schnering, and J. Pannetier, Rev. Phys. Appl. **19**, 807 (1984).
[29] F. Liu, P. Parajuli, R. Rao, P. C. Wei, A. Karunarathne, S. Bhattacharya, R. Podila, J. He, B. Maruyama, G. Priyadarshan, J. R. Gladden, Y. Y. Chen, and A. M. Rao, Phys. Rev. B **98**, 224309 (2018).

[30] C. Chang, M. Wu, D. He, Y. Pei, C.-F. Wu, X. Wu, H. Yu, F. Zhu, K. Wang, Y. Chen, L. Huang, J.-F. Li, J. He, and L.-D. Zhao, Science **380**, 778 (2018).

[31] L.-D. Zhao, G. Tan, S. Hao, J. He, Y. Pei, H. Chi, H. Wang, S. Gong, H. Xu, V. P. Dravid, C. Uher, G. J. Snyder, C. Wolverton, and M. G. Kanatzidis, Science **351**, 6269 (2015).

[32] G. Schuck, D. M. Tobbens, M. Koch-Muller, I. Efthimiopoulos, and S. Schorr, J. Phys. Chem. C **122**, 5227 (2018).

[33] R. Trittschack, B. Grobety, and M. Koch-Muller, Amer. Miner. **97**, 1965 (2012).

[34] K. Syassen, High Press. Res. **28**, 75 (2008).

[35] H.-P. Liermann, Z. Konopkova, W. Morgenroth, K. Glazyrin, J. Bednarcik, E. E. McBride, S. Petitgirard, J. T. Delitz, M. Wendt, Y. Bican, A. Ehnes, I. Schwark, A. Rothkirch, M. Tischer, J. Heuer, H. Schulte-Schrepping, T. Kracht, and H. Franz, J. Synchrotron Rad. **22**, 908 (2015).

[36] A. P. Hammersley, S. O. Svensson, M. Hanfland, A. N. Fitch, and D. Hausermann, High Pres. Res. **14**, 235 (1996).

[37] B. H. Toby, J. Appl. Crystallogr. **34**, 210 (2001).

[38] D. Errandonea, R. Boehler, S. Japel, M. Mezouar, and L. R. Benedetti, Phys. Rev. B **73**, 092106 (2006).

[39] M. Ross, H. K. Mao, P. M. Bell, and J. A. Xu, J. Chem. Phys. **85**, 1028 (1986).

[40] R. Dovesi, R. Orlando, A. Erba, C. M. Zicovich-Wilson, B. Civalleri, S. Casassa, L. Maschio, M. Ferrabone, M. De La Pierre, P. D'Arco, Y. Noël, M. Causà, M. Rérat, and B. Kirtman, International Journal of Quantum Chemistry **114**, 1287 (2014).

[41] R. Dovesi, V. R. Saunders, C. Roetti, R. Orlando, C. M. Zicovich-Wilson, F. Pascale, B. Civalleri, K. Doll, N. M. Harrison, I. J. Bush, P. D'Arco, M. Llunell, M. Causà, and Y. Noël, "CRYSTAL14 User's Manual," University of Torino: Torino, 2014.

[42] J. P. Perdew, A. Ruzsinszky, G. I. Csonka, O. A. Vydrov, G. E. Scuseria, L. A. Constantin, X. Zhou, and K. Burke, Phys. Rev. Lett. **100**, 136406 (2008).

[43] C. Adamo and V. Barone, J. Chem. Phys. **110**, 6158 (1999), https://doi.org/10.1063/1.478522.

[44] J. P. Perdew, K. Burke, and M. Ernzerhof, Phys. Rev. Lett. **77**, 3865 (1996).

[45] M. Towler and C. Zicovich-Wilson, "Selenium basis sets for the crystal program," (1995).

[46] G. Sophia, *Ab-initio study of the dielectric response of high-permittivity perovskites for energy storage*, Ph.D. thesis, Univesité de Pau et des Pays de l'Adour and Università degli Studi di Torino, Turin (2014).

[47] B. Metz, H. Stoll, and M. Dolg, J. Chem. Phys. **113**, 2563 (2000).

[48] "Supplementary infromation available at:,".

[49] F. Pascale, C. M. Zicovich-Wilson, F. López Gejo, B. Civalleri, R. Orlando, and R. Dovesi, Journal of Computational Chemistry **25**, 888, https://onlinelibrary.wiley.com/doi/pdf/10.1002/jcc.20019.

[50] C. M. Zicovich-Wilson, F. Pascale, C. Roetti, V. R. Saunders, R. Orlando, and R. Dovesi, Journal of Computational Chemistry **25**, 1873 (2004), https://onlinelibrary.wiley.com/doi/pdf/10.1002/jcc.20120.

[51] K. Doll, Molecular Physics **108**, 223 (2010), https://doi.org/10.1080/00268970903193028.

[52] M. Ferrero, M. Rérat, R. Orlando, and R. Dovesi, Journal of Computational Chemistry **29**, 1450 (2008), https://onlinelibrary.wiley.com/doi/pdf/10.1002/jcc.20905.

[53] M. Ferrero, M. Rérat, B. Kirtman, and R. Dovesi, J. Chem. Phys. **129**, 244110 (2008), https://doi.org/10.1063/1.3043366.

[54] R. Orlando, V. Lacivita, R. Bast, and K. Ruud, J. Chem. Phys. **132**, 244106 (2010).

[55] L. Maschio, B. Kirtman, R. Orlando, and M. Rérat, J. Chem. Phys. **137**, 204113 (2012), https://doi.org/10.1063/1.4767438.

[56] H. R. Chandrasekhar, R. G. Humphreys, U. Zwick, and M. Cardona, Phys. Rev. B **15**, 2177 (1977).

[57] C. Julien, M. Eddrief, I. Samaras, and M. Balkanski, Mater. Sci. Eng. B **15**, 70 (1992).

[58] Q. Lu, M. Wu, D. Wu, C. Chang, Y.-P. Guo, C.-S. Zhou, W. Li, X.-M. Ma, G. Wang, L.-D. Zhao, L. Huang, C. Liu, and J. He, Phys. Rev. Lett. **119**, 116401 (2017).

[59] I. Loa, S. R. Popuri, A. D. Fortes, and J. W. G. Bos, Phys. Rev. Materials **2**, 085405 (2018).

[60] P. M. Nikolic, L. Milkovic, P. Mihajlovic, and B. Lavrencic, Czech. J. Phys. B **28**, 456 (1978).

[61] S. Luo, X. Qi, H. Yao, X. Ren, Q. Chen, and J. Zhong, J. Phys. Chem. C **121**, 4674 (2017).

[62] J. Zhang, H. Zhu, X. Wu, H. Cui, D. Li, J. Jiang, C. Gao, Q. Wang, , and Q. Cui, Nanoscale **7**, 10807 (2015).

[63] O. Chaix-pluchery, L. Abello, G. Lucazeau, B. Chenevier, and R. Madar, J. Phys. Chem. Solids **57**, 527 (1996).

[64] G. Lucazeau, J. Raman Spectr. **34**, 478 (2003).

[65] D. L. Mills, A. A. Maradudin, and E. Burstein, Annals of Physics **56**, 504 (1970).

[66] A. F. Goncharov and V. V. Struzhkin, J. Raman Spectr. **34**, 532 (2003).

[67] G. A. Kourouklis and E. Anastassakis, Phys. Stat. Sol. (b) **152**, 89 (1989).

[68] G. Liu, J. Zhou, and H. Wang, Phys. Chem. Chem. Phys. **19**, 15187 (2017).

[69] S. Alptekin, J. Mol. Model. **17**, 2989 (2011).

[70] L. A. Davis and R. B. Gordon, J. Chem. Phys. **46**, 2650 (1967).

[71] D. Zhou, Q. Li, W. Zheng, Y. Ma, and C. Chen, Phys. Chem. Chem. Phys. **19**, 4560 (2017).

[72] S. Baroni, S. de Gironcoli, A. D. Corso, and P. Giannozzi, Rev. Mod. Phys. **73**, 515 (2001).

[73] L. Makinistian and E. A. Albanesi, Comput. Mater. Sci. **50**, 2872 (2011).

[74] P. S. Peercy and B. Morosin, Phys. Rev. B **7**, 2779 (1973).

[75] M. Balkanski, R. F. Wallis, and E. Haro, Phys. Rev. B **28**, 1928 (1983).

[76] P. G. Klemens, Phys. Rev. B **148**, 845 (1966).

[77] Z. Zhao, J. Elwood, and M. A. Carpenter, J. Phys. Chem. C **119**, 23094 (2015).

[78] L. Su, Y. Zhang, Y. Yu, and L. Cao, Nanoscale **6**, 4920 (2014).

[79] R. L. Gonzalez-Romero, A. Antonelli, and J. J. Melendez, Phys. Chem. Chem. Phys. **19**, 12804 (2017).

[80] J. Hong and O. Delaire, arxiV: 1604.07077v2 (2016).

[81] K. Kutorasinski, B. Wiendlocha, S. Kaprzyk, and J. Tobola, Phys. Rev. B **91**, 205201 (2015).

[82] J. Peng, W. Li, Y. Wang, X. Yu, J. Liu, and Q. He, J. Mol. Model. **23**, 319 (2017).

[83] D. Olego, M. Cardona, and P. Vogl, Phys. Rev. B **25**, 3878 (1982).

[84] A. R. Goni, H. Siegle, K. Syassen, C. Thomsen, and J.-M. Wagner, Phys. Rev. B **64**, 035205 (2001).

[85] J. S. Reparaz, K. P. da Silva, A. H. Romero, J. Serrano, M. R. Wagner, G. Callsen, S. J. Choi, J. S. Speck, and A. R. Goni, Phys. Rev. B **98**, 165204 (2018).

[86] J. S. Reparaz, L. R. Muniz, M. R. Wagner, A. R. Goni, M. I. Alonso, A. Hoffmann, and B. K. Meyer, Appl. Phys. Lett. **96**, 231906 (2010).

[87] J. A. V. Vechten, Phys. Rev. **182**, 891 (1969).

[88] R. B. Shalvoy, G. B. Fisher, and P. J. Stiles, Phys. Rev. B **15**, 1680 (1977).

[89] P. J. Stiles, Sol. St. Comm. **11**, 1063 (1972).

Appendix A: Effects of n- and p-type doping on the structural, vibrational, and optical properties of SnSe

Adding to our aforementioned studies, we have investigated the effect of n- and p-type doping on the structural, vibrational, and optical properties of pristine/non-doped SnSe at ambient conditions. The relevant synthesis details of the probed single-crystalline Br-doped SnSe (n-type $SnSe_{0.97}Br_{0.03}$) and Na-doped SnSe (p-type $Sn_{0.985}Na_{0.015}Se$) are reported elsewhere [30, 31]. In Fig. 10 we present first the collected XRD patterns and the corresponding Raman spectra for the various SnSe samples. From these measurements, it is evident that this amount of either Na- or Br-doping does not have any visible effect on either the long-range (XRD) or local (Raman) structural properties of SnSe.
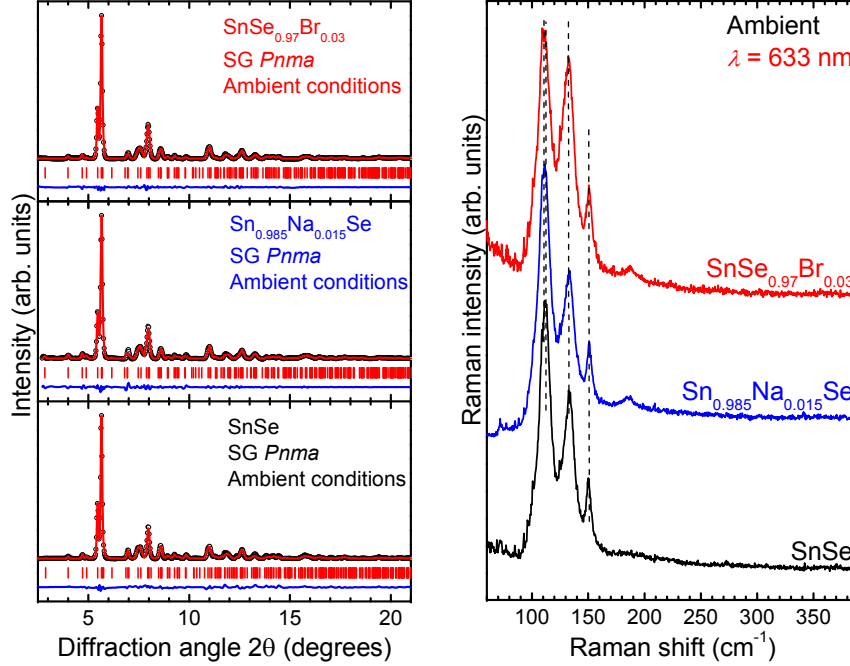
FIG. 10: (Left) Rietveld refined XRD patterns for the non-doped, the Na/p-doped, and the Br/n-doped SnSe samples measured at ambient conditions ($\lambda = 0.29$ Å). The black circles and the red solid lines correspond to the measured and the fitted patterns, whereas their difference is depicted as blue lines. Vertical ticks mark Bragg peak positions. (Right) Raman spectra for the non-doped, the Na/p-doped, and the Br/n-doped SnSe samples at ambient conditions ($\lambda = 633$ nm).

On the other hand, our optical investigations show pronounced differences between the various samples. In Fig. 11 we display the experimental FIR reflectance spectra at RT collected along the *b*- and *c*-axis for the various samples (left column), alongside the derived real and imaginary parts of optical conductivity $\sigma(\omega) = \sigma_1(\omega) + i\sigma_2(\omega)$. For the non-doped SnSe sample, both the TO phonons with Lorentzian lineshapes in the $\sigma_1(\omega)$ spectra, and the corresponding dispersive features in $\sigma_2(\omega)$ are apparent. For the Br/n-doped sample, the lineshapes become more asymmetric in the $\sigma_1(\omega)$ spectra (Fano effect), whereas the TO phonons are screened by the introduction of additional free carriers due to the doping process (electron-phonon interaction). In the Na/p-doped SnSe sample on the other hand, the electron screening of the TO phonons in the respective $\sigma_1(\omega)$ spectra is much stronger, owing to a much higher carrier density turning leading to a metallic behavior; a standard Drude component could not clearly detected in this case, however. All in all, our optical investigations are in line with the corresponding electrical conductivity/resistivity measurements on these samples [30, 31, 58].

Finally we mention that this amount of n- or p-type doping does not influence either the $Pnma \rightarrow Bbmm$ transition temperature at ambient pressure [30, 31], or the transition pressure at ambient temperature (the latter derived from our high-pressure Raman measurements not shown here).
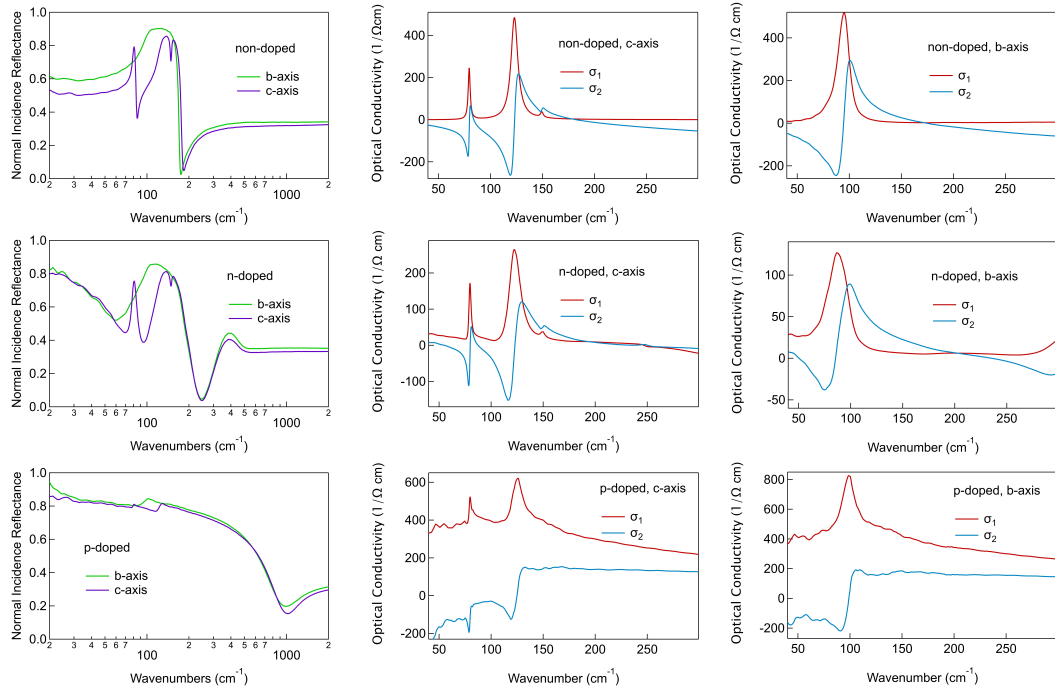
FIG. 11: Experimental reflectance spectra at ambient conditions for the *b*- and *c*-axes (left column), alongside the derived optical conductivities $\sigma = \sigma_1 + i\sigma_2$ for the undoped and doped SnSe samples.